ACS APPLIED NANO MATERIALS

www.acsanm.org Article

Single-Walled Carbon Nanotubes as One-Dimensional Scattering Surfaces for Measuring Point Spread Functions and Performance of Tip-Enhanced Raman Spectroscopy Probes

Luke R. McCourt,* Ben S. Routley, Michael G. Ruppert, Vicki J. Keast, C. I. Sathish, Rohan Borah, Renee V. Goreham, and Andrew J. Fleming

Cite This: *ACS Appl. Nano Mater.* 2022, 5, 9024−9033 Read Online

ACCESS | Metrics & More | Article Recommendations | Supporting Information

ABSTRACT: This Article describes a method for the characterization of the imaging performance of tip-enhanced Raman spectroscopy probes. The proposed method identifies single-walled carbon nanotubes that are suitable as one-dimensional Raman scattering objects by using atomic force microscope maps and exciting the radial breathing mode using 785 nm illumination. High-resolution cross sections of the nanotubes are collected, and the point spread functions are calculated along with the optical contrast and spot diameter. The method is used to characterize several probes, which results in a set of imaging recommendations and a summary of limitations for each probe. Elemental analysis and boundary element simulations are used to explain the formation of multiple peaks in the point spread functions as a consequence of random grain formation on the probe surface.

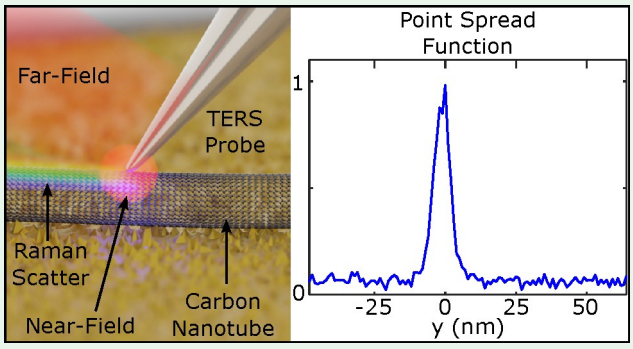

KEYWORDS: *TERS, enhancement, near-field, Raman, spectroscopy, point spread function*

INTRODUCTION

Tip-enhanced Raman spectroscopy (TERS) is an imaging technique that allows subdiffraction limited imaging of surfaces with the chemical sensitivity of Raman spectroscopy.[1] Figure 1 illustrates the basic operation principle of TERS in the side illumination configuration as a silver atomic force microscope (AFM) probe is scanned over a single-walled carbon nanotube (SWCNT) on a gold substrate. The focused laser excites collective oscillations of the surface electrons, known as surface plasmons, resulting in charge accumulation at the tip apex.[2,3] The charge accumulations produce an electric near-field that is enhanced in magnitude and localized to the surface.[4] The enhanced near-field increases the inelastic Raman scattering from the sample in the subdiffraction limited near-field spot.[5,6] TERS has been used to provide chemical mapping of surfaces below the optical diffraction limit for applications including sample characterization during chemical synthesis and imaging of biological samples.[7−9]

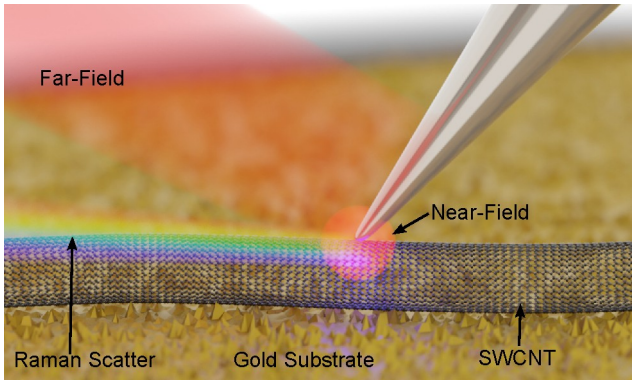

Figure 1. Illustration of tip-enhanced Raman scattering from a silver probe on a single-walled carbon nanotube.

Tip design is paramount for high enhancement and spatial resolution.[10,11] The formation of plasmon modes is dependent on material and geometry.[12] The most common probe surface material is silver due to the low plasmon losses, particularly at blue-green wavelengths.[13] Gold can be used as an alternative due to its superior chemical stability, despite lower reported enhancement.[14] The plasmon resonance wavelength is generally tunable with particle length, while the enhancement

Received: March 23, 2022
Accepted: June 6, 2022
Published: June 21, 2022

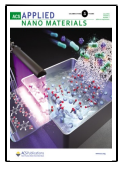

Downloaded via UNIV OF NEWCASTLE on February 13, 2023 at 11:03:27 (UTC).
See https://pubs.acs.org/sharingguidelines for options on how to legitimately share published articles.

ACS Publications © 2022 American Chemical Society

https://doi.org/10.1021/acsanm.2c01274
ACS Appl. Nano Mater. 2022, 5, 9024−9033

is improved with apex sharpness.[15−17] Metal coated probes rely on a grainy surface to create enhancing nanoparticles. As a result, the spatial resolution and enhancement is dependent on the formation of a suitable grain structure at the tip apex.[18] A thick metal layer has been shown to increase the likelihood of particle formation at the tip apex, which produces a hot spot at the apex.[19]

Tip−sample interactions also effect enhancement and spatial resolution. Further spatial confinement and increased enhancement are achieved with plasmon-excition coupling[20,21] and the formation of tip−sample−tip gap modes,[22−24] while at small tip−sample separations quantum effects begin to reduce confinement.[25] Furthermore, the substrate geometry influences the enhancement and spatial resolution. Similar to surface-enhanced Raman spectroscopy, the presence of sharp metal edges on the substrate has been shown to amplify Raman enhancement through nonresonant and plasmon effects. For example, the enhancement and spatial resolution are improved at the edges of gold nanodisks.[26] In addition, the sample chemistry influences the scattering efficiency. For example, predominantly, covalent nanoparticles have been shown to have significantly higher scattering cross sections compared to ionic nanoparticles due to an increased polarizability, resulting in a 2 orders of magnitude increase in the enhancement factor.[27] Highly anisotropic molecules such as nanotubes are sensitive to polarization.[28] Finally, Raman enhancement has been shown to be dependent on conduction electron properties.[29,30]

Finite element simulations can be used to estimate the enhancement factor, and these values are often quoted by probe manufacturers.[26,31,32] However, approximations for probe and sample geometry are often required, reducing the validity of simulations as surface plasmons are sensitive to surface morphology including fine grain structure.[33,34] Furthermore, Raman enhancement values from these simulations are often not indicative of laboratory performance.

The enhancement factor, F, is often used to characterize the Raman enhancement and is given by[35]

$$F = \left(\frac{I_{\mathrm{nf}} - I_{\mathrm{ff}}}{I_{\mathrm{ff}}} - 1\right)\frac{V_{\mathrm{ff}}}{V_{\mathrm{nf}}} \tag{1}$$

where I_{nf} and I_{ff} are the near-field and far-field intensities and V_{nf} and V_{ff} are the near-field and far-field volumes. The far-field intensity is collected with the tip retracted and the near-field, with the tip on the sample. The far-field volume is often estimated as the diffraction limited spot size of the illumination laser[36−39] and the near-field volume, by the tip apex diameter.[36,37] There are several modifications of eq 1 that account for factors such as the number of molecules in each scattering volume[40] or the tip acting as a mirror.[38] For a given enhancement factor, a larger near-field volume of the same intensity will result in a higher near-field signal. Alternatively, the contrast can be defined as $I_{\mathrm{nf}}/I_{\mathrm{ff}}$, which more accurately quantifies the measured near-field to far-field signal ratio. The literature contains many values of the contrast, which has also been summarized.[41]

For TERS imaging, rather than point spectroscopy, different methods can be used to characterize the TERS system. In an optical system, the point spread function (PSF) describes the response to a point light source. Images formed using a given system are the convolution of the PSF and the true image.[42] For TERS, the spot diameter of the PSF defines the spatial resolution, which depends on the volume of the near-field in the tip−sample junction.[25] The image contrast is determined by $I_{\mathrm{nf}}/I_{\mathrm{ff}}$ where the near-field signal is collected on a sample molecule and the far-field signal is collected on the substrate. The image contrast quantifies the systems ability to distinguish features on the sample. Hence, the PSF characterizes the TERS imaging performance of a system.

To measure the PSF, a scattering object that approximates a delta function is required.[42] Single-walled carbon nanotubes (SWCNTs) act as one-dimensional scattering structures with diameters on the order of 1 nm and lengths that may exceed 1 μm.[43,44] This makes SWCNTs superior for TERS characterization compared to most nanoparticles that are typically on the order of tens of nanometers in diameter. Thus, SWCNTs are suitable structures for the measurement the PSFs of TERS probes. Furthermore, the length of the SWCNTs allows repeat measurements of the same structure from a single TERS image.

SWCNTs have three major spectral bands of interest, the radial breathing mode (RBM), D-band, and G-band. The D-band and G-band occur at around 1350 and 1582 cm^{-1}, respectively, and the D-band magnitude is associated with defects. The RBM wavenumber is dependent on tube diameter; a simple model is given by

$$\omega_{\mathrm{RBM}} = \frac{A}{d_{\mathrm{t}}} + B \tag{2}$$

where A is typically around 248 cm^{-1} and B accounts for environmental factors such as the surrounding medium, nanotube bundling, molecular adsorption, and surfactant, which all affect the wavenumber and intensity of the RBM.[45] Hence, an analysis of the RBM wavenumber distribution allows the distribution of the diameters to be determined. This model is accurate for SWCNTs on the order of 1 nm, while for larger diameters, the RBM is hardly observable.[46,47]

SWCNTs are not ideal for measuring the PSF of a TERS system, as the scattering cross sections are dependent on the environment surrounding the nanotube and the polarization. It has been shown that SWCNTs on a glass substrate only respond to light polarized parallel to the tube axis.[28] The absorption of light polarized parallel to the tube axis has been found to be 20 times greater than that of the perpendicular polarized light due to the extreme anisotropic nature of the SWCNTs.[48] In addition, the RBM signal increases as the chiral angle decreases.[49] However, the one-dimensional nature and availability of the SWCNTs make them accessible scattering objects for the measurement of the PSF of the TERS systems. Furthermore, the impact of environment and chirality on the measured results can be controlled using a single sample for all probes that will be compared.

SWCNTs have been used previously to measure the resolution of TERS systems.[50] SWCNTs have also been used to fit Gaussian functions to the near- and far-fields for bottom illumination TERS.[38] In doing so, the enhancement factor and optical spot size were determined. However, the height map range of 1 μm indicates that bundles of nanotubes were imaged. Similarly, nanotube bundles have been imaged, and the bundle width was used to estimate the enhancement factor.[51]

This Article describes a method for the measurement of the PSF of TERS probes using SWCNTs. The RBM of the SWCNTs is analyzed to identify single nanotubes. High-resolution TERS cross sections of the SWCNTs are collected, and the PSF is calculated. From the PSF, the contrast and spot

https://doi.org/10.1021/acsanm.2c01274
ACS Appl. Nano Mater. 2022, 5, 9024−9033

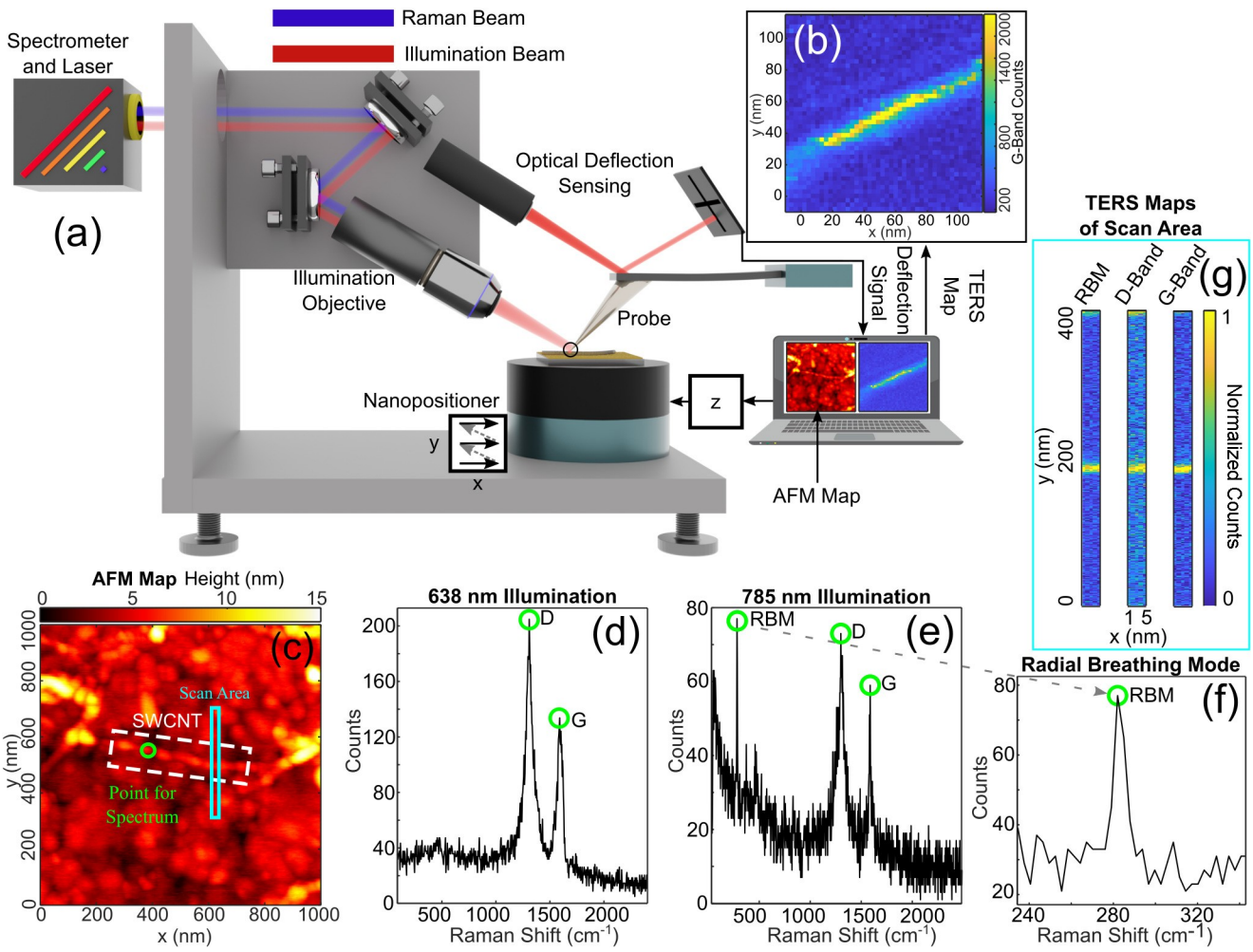

Figure 2. (a) Schematic of the experimental setup used for TERS. The side illumination setup requires TERS probes with the access tip geometry as shown. (b) The TERS map shows the G-band counts of a single-walled carbon nanotube (SWCNT). (c) An AFM map of a SWCNT that is suitable for collecting TERS cross sections. The nanotube (surrounded by the white box) is approximately aligned horizontally. The spectrum of the SWCNT is collected to ensure the radial breathing mode (RBM) is present when illuminated with the 785 nm laser. The scan area (shown by the cyan box) is 400 × 5 nm with a pixel size of 1 nm^2. (d, e) Example TERS spectra of a SWCNT for 785 and 638 nm illumination. (f) A zoomed plot of the RBM peak at 285 cm^{-1}. (g) Example TERS cross sections plotted for the RBM, D-band, and G-band. These cross sections are used to calculate the PSF, contrast, and spot diameter of the TERS probes.

diameter are calculated, allowing a comparison of the imaging performance. This is repeated with 638 and 785 nm laser excitation to quantify probe performance at these two wavelengths, which are commonly used for TERS imaging of different materials.

METHOD

Sample Preparation. Polished silicon substrates were coated with a 50 nm thick gold layer using thermal evaporation. (6,5)-Chirality SWCNTs were purchased (Signis SG65i) with a reported average diameter of 0.78 nm as measured using near-infrared fluorescence spectroscopy. The nanotubes were dispersed in *N*-methyl-2-pyrrolidone with an initial mass loading of 1 mg/mL. The mixture was bath sonicated for 15 min. The initial mass loading was found to be too high as a sediment was formed. The mixture was diluted 10-fold and bath sonicated for 15 min. The translucent decantate of this mixture was further diluted 5-fold and sonicated for 15 min. The solution was drop cast onto the gold substrate, which was held horizontal using reverse action forceps and was left to dry for several days.

TERS. Figure 2a shows a schematic of the TERS microscope used for this work. The Horiba XploRA Plus confocal Raman microscope provides the spectrometer and filters to process the Raman scattered light collected from the sample. The XploRA unit also provided the 785 nm laser excitation. The system was modified to include a 638 nm fiber coupled laser. The microscope operates with side illumination, where the laser is focused onto the tip apex using a 100×, 0.7 numerical aperture side objective lens. A laser power of 0.7 mW measured at the probe results in a power density of approximately 4.3 × 10^5 W/cm^2 for the 638 nm laser and 2.8 × 10^5 W/cm^2 for the 785 nm laser. Both laser sources were aligned with a vertical polarization. The laser alignment procedure is detailed in Figure S1. A 600 g/mm grating resulted in a spectral resolution of 3.1 cm^{-1}.

An AIST-NT AFM was used to control the tip scanning. The used scanning protocol was a hybrid mode where the Raman signal is collected in contact mode for the specified acquisition time. The height map and movement between pixels are performed in tapping mode. The Raman acquisition time was minimized while achieving an acceptable Raman signal-to-noise and was generally 0.1−0.5 s. This reduced the duration of mapping and avoided unnecessary optical drift. An example G-band TERS map of a SWCNT is shown in Figure 2b.

AFM maps were acquired using tapping mode to minimize sample and probe damage. These AFM maps are used to identify suitable carbon nanotubes that appear as isolated tubes, free from any bundles,

https://doi.org/10.1021/acsanm.2c01274
ACS Appl. Nano Mater. 2022, 5, 9024−9033

and are roughly aligned with the x-axis. An example of a suitable SWCNT is shown in Figure 2c. Once a suitable SWCNT is found, the tip is put into contact with the nanotube and the laser alignment is adjusted to optimize the Raman signal. The Raman signal is checked for the presence of a single radial breathing mode peak at approximately 280 cm^{-1}. A narrow line width supports the conclusion that this is an isolated SWCNT. If this peak is not present or appears to be broadened or there are multiple peaks, then the CNT is deemed unsuitable and another is found. If a Raman spectrum typical of a SWCNT cannot be produced, the TERS probe is deemed to have failed. Example SWCNT spectra for 638 and 785 nm excitation are shown in Figure 2d,e where the RBM mode occurs at 288 cm^{-1}, the D-band occurs at 1289 cm^{-1}, and the G-band occurs at 1587 and 1580 cm^{-1} for 638 and 785 nm excitation, respectively. The RBM is only excited with the 785 nm excitation. A zoomed plot of the RBM is shown in Figure 2f.

For a suitable SWCNT, a TERS map is acquired with an area of 5 nm × 400 nm with the long axis aligned perpendicular to the SWCNT and a pixel count of 5 × 400. The map contains 5 cross sections of the SWCNT. Examples of RBM, D-band, and G-band TERS maps are shown in Figure 2g with the SWCNT occurring at approximately y = 200.

For a given wavenumber ω, let the Raman map be denoted as

$$M_\omega = \begin{bmatrix} m_{1,1} & \cdots & m_{1,400} \\ \vdots & \ddots & \vdots \\ m_{5,1} & \cdots & m_{5,400} \end{bmatrix} \tag{3}$$

where $m_{i,j}$ are the Raman counts at each pixel and each row has been aligned so that the SWCNT is positioned approximately at index 200. When one assumes the PSF is symmetric in the x-axis and y-axis

$$\mathrm{PSF}_{\omega,j} = \frac{\sum_{i=1}^{5} m_{i,j}}{\max\left(\sum_{i=1}^{5} m_{i,j}\right)} \tag{4}$$

The far-field contribution is estimated by taking the mean of the PSF with the near-field peak removed:

$$\overline{\mathrm{PSF}}_{\mathrm{ff}} = \frac{\sum_{j=1}^{l} \mathrm{PSF}_{\omega,j} + \sum_{j=r}^{\mathrm{end}} \mathrm{PSF}_{\omega,j}}{n} \tag{5}$$

where l and r are the j indices at two full maximums to the left and right of the PSF peak, respectively, and n is the number of elements in the numerator.

The near-field PSF is then

$$\mathrm{PSF}_{\mathrm{nf}} = \mathrm{PSF} - \overline{\mathrm{PSF}}_{\mathrm{ff}} \tag{6}$$

The contrast is calculated as

$$C_\omega = \frac{1 - \overline{\mathrm{PSF}}_{\mathrm{ff}}}{\overline{\mathrm{PSF}}_{\mathrm{ff}}} \tag{7}$$

which quantifies the ratio of near-field to far-field contributions. Hence, a high contrast will allow objects of interest to be distinguished from the substrate. The starting wavenumbers were 285 cm^{-1} for the RBM, 1292 cm^{-1} for the D-band, and 1606 cm^{-1} for the G-band. The wavenumbers were adjusted to maximize the contrast for each band. The mean contrast is calculated across the spectral bands to reduce the effects of band ratio variation between the nanotubes. For 638 nm excitation, the RBM is not included in the calculation as it is not effectively excited at this wavelength. The mean contrasts are

$$\bar{C}_{785} = \frac{C_{\mathrm{RBM}} + C_{\mathrm{D}} + C_{\mathrm{G}}}{3} \tag{8}$$

and

$$\bar{C}_{638} = \frac{C_{\mathrm{D}} + C_{\mathrm{G}}}{2} \tag{9}$$

From eq 6, the spot diameter d is the diameter where $\mathrm{PSF}_{\mathrm{nf}}$ falls to $1/e^2$ of the maximum value. This procedure was repeated using 785 and 638 nm lasers. The data processing method is summarized in the flowchart provided Figure S3. In this work, contrast and spot diameter are the metrics that characterize the imaging the performance of a TERS system.

TERS Probes. Three commercially available probes were selected to demonstrate the method presented in this Article:

- A: silver and gold coated silicon
- B: gold coated silicon
- C: gold coated silicon

Silver tarnishes rapidly in ambient conditions, which results in a redshift in plasmon energy and a decreased scattering cross section.[52−55] Hence, the silver probes were kept in the sealed packages they were delivered in and were opened immediately before use. This minimized the possibility of silver degradation. The Au probes were stored in gel packs in ambient conditions.

SEM and EDX. A JEOL FE-SEM was used for SEM imaging and EDX element analysis. EDX was performed where the probe was thick enough to limit the effects associated with a finite electron penetration depth and allow a comparison between the probes. The SEM and EDX were performed immediately after opening the sealed packages. These probes were not used for TERS, as enhancement was found to degrade after SEM/EDX, likely due to carbon contamination. An example SEM image is shown in Figure 3 with the EDX area indicated.

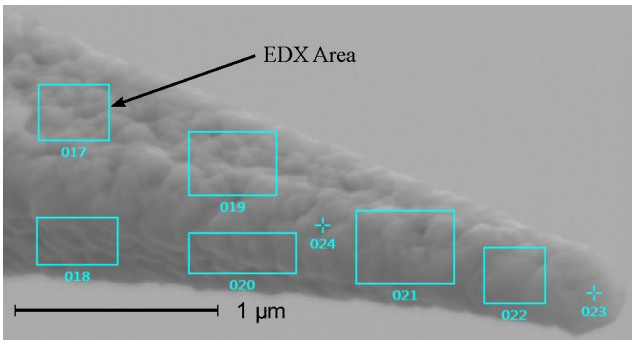

Figure 3. SEM image of a probe showing the EDX area of analysis.

Simulations. Boundary element method simulations were performed to investigate the role of random grain formation on the PSF of TERS probes. These simulations were performed using the MNPBEM MATLAB package.[56] 638 nm plane wave excitation was incident on silver nanocones with an apex diameter of 40 nm. To simulate different grain formations at the tip apex of TERS probes, several configurations of silver nanospheres with 30 nm diameters were embedded into the nanocones. Electric field maps were calculated and analyzed.

RESULTS

SEM Images and EDX Element Analysis. SEM images of the tested TERS probes are shown in Figure 4. The apex radius was estimated using the SEM images with the assumption that the tip apex is a nanosphere. The element compositions of the probes as measured using EDX are given in Table 1. Probe A has the largest apex diameter at 430 nm. This corresponds to the highest metal composition by percentage of mass at 90%, consisting of 73% silver and 7% gold. Probes B and C both have smaller apex diameters at 147 and 203 nm, respectively. Probes A, B, and C have visible metal grain structures on their surfaces and have metal contents exceeding 70%.

Imaging Performance. The wavenumbers that maximized the contrast for each probe are given in Table 2. Using probe

https://doi.org/10.1021/acsanm.2c01274
ACS Appl. Nano Mater. 2022, 5, 9024−9033

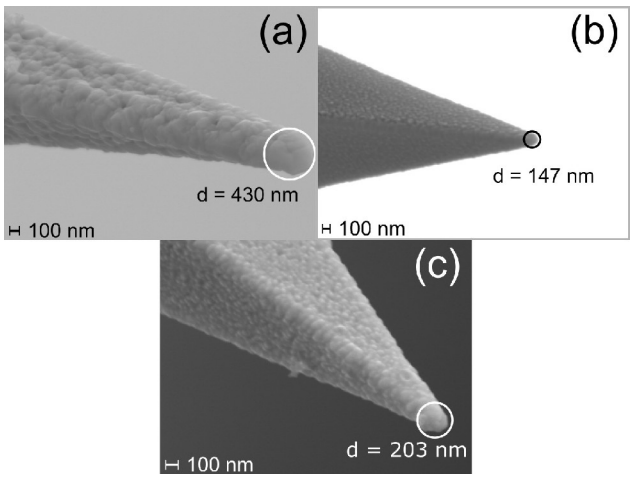

Figure 4. SEM images of the TERS probes reviewed in this paper: (a) probe A, (b) probe B and (c) probe C. The approximate apex diameters are displayed on each image.

Table 1. Mass Composition of TERS Probes Measured Using EDX

probe	silicon (mass %)	silver (mass %)	gold (mass %)
A	12	73	7
B	3	0	86
C	19	0	72

Table 2. Wavenumbers That Maximized the Contrast for Each Spectral Band and Probe

probe	wavelength (nm)	RBM (cm^{-1})	D-band (cm^{-1})	G-band (cm^{-1})
A	638	N/A	1325	1602
	785	282	1302	1585
B-1	638	N/A	1289	1587
B-2	785	288	1289	1580
C-1	638	N/A	1313	1594
C-2	785	285	1284	1587

A, the data for 638 and 785 nm excitation was successfully collected with a single probe. For probes B and C, two probes each were required as probe degradation occurred while searching for suitable SWCNTs after switching from 785 to 638 nm excitation.

Figure 5 shows the PSFs for the RBM, D-band, and G-band for probes A, B, and C with 638 and 785 nm illumination. The contrast for each band, the calculated spot diameters and the apex diameter estimated from the SEM data are summarized in Table 3. Of the probes tested, probe A provides the highest contrast with 638 and 785 nm excitation, which require shorter acquisition times than the other probes tested. However, the spot diameter is also the largest at 57 and 52 nm for 638 and 785 nm excitation, respectively. This makes probe A suitable for high-speed, lower resolution TERS imaging. However, the PSFs reveal multiple hot spots, which introduce artifacts into the TERS maps. This appears as a ghosting effect in the TERS maps to the right of the SWCNT in Figure 5a−c and the left in Figure 5m−o.

Probe B-1 provides poor contrast with 638 nm excitation. Hence, long acquisition times are required for an acceptable signal-to-noise ratio. Furthermore, the spot diameter of 45 nm and multiple hot spots make the probe unsuitable for high-resolution imaging. Conversely, probe B-2 provides adequate contrast at 785 nm excitation, the narrowest spot diameter at 16 nm, and a single hot spot, which make the probe suitable for high-speed, high-resolution imaging.

Probe C-1 provides adequate contrast at 638 nm excitation and a spot diameter of 28 nm, making it the most suitable for high-speed, high-resolution imaging. However, the PSF of probe C-1 shows multiple hot spots, which will result in ghosting artifacts that are visible in the TERS maps shown in Figure 5h,i. Probe C-2 provides a lower contrast at 785 nm excitation compared to probe B-2 and, thus, is less suitable for high-speed imaging. To compensate for the lower contrast, longer acquisition times will be necessary. However, long acquisition times introduce significant optical drift and expose the probe to an extended period of illumination that may degrade the metal layer. On the other hand, the spot diameter is relatively small and the PSFs show one hotspot making probe C-2 suitable for low-speed high-resolution imaging.

The measured spot diameters are significantly smaller than the apex diameters. For example, probe A has a measured spot diameter of 57 nm when excited with the 638 nm laser, while the apex diameter is approximately 430 nm. Thus, for this example, the spot diameter is only 13% of the apex diameter, which is much smaller than previously reported.[57] This shows that approximating the tip apex as a sphere for a grainy probe is inadequate for the estimation of the spatial resolution. The complex geometry at the tip apex must be considered along with tip−sample interactions that increase confinement.[22−24] As an example, Figure 4c shows sharp features at the tip apex that are smaller than the apex diameter if the tip is considered as a sphere. It is possible that higher resolution SEM images would reveal further features at the tip apex.

Random grain formation can partially explain the differences in PSFs between probes B-1 and B-2, likewise between C-1 and C-2. The grain formation at the tip apex will determine the spot diameter, and this will vary from probe to probe.[18] However, probe A also displays different PSFs when illuminated with 638 and 785 nm excitation despite being the same probe. One explanation is that different plasmon modes are being excited that have unique enhancement distributions. This effect has been demonstrated on gold nanoparticles in the literature.[58,59] Another potential explanation is that the tip morphology was altered due to excessive heat generation, although anecdotally this is usually associated with a significant decrease in enhancement and therefore unlikely.

There are notable differences between the PSFs of the spectral bands for probe C when illuminated with the 638 nm laser. The D-band PSF displays two distinct peaks while the G-band PSF displays a less pronounced second peak as shown in Figure 5h,i, respectively. This is undesirable as it indicates that the choice of spectral band effects the measured PSF. This effect is not present for the other measurements presented. It is possible that a bundle of nanotubes were imaged with individual nanotubes of varying D-band and G-band scattering cross sections.

The presented method allows the PSF to be measured when $d_{SWCNT} \ll d_{spot}$, where d_{SWCNT} is the SWCNT diameter and d_{spot} is the PSF spot diameter.[42] This inequality is true for the conditions described in this Article. However, the method is likely to be unsuitable for the measurement of the PSF of TERS systems that exhibit subnanometer resolution where $d_{SWCNT} \approx d_{spot}$, such as those under vacuum.[22,60] Furthermore, as SWCNTs are only excited by in-plane polarizations, the

https://doi.org/10.1021/acsanm.2c01274
ACS Appl. Nano Mater. 2022, 5, 9024−9033

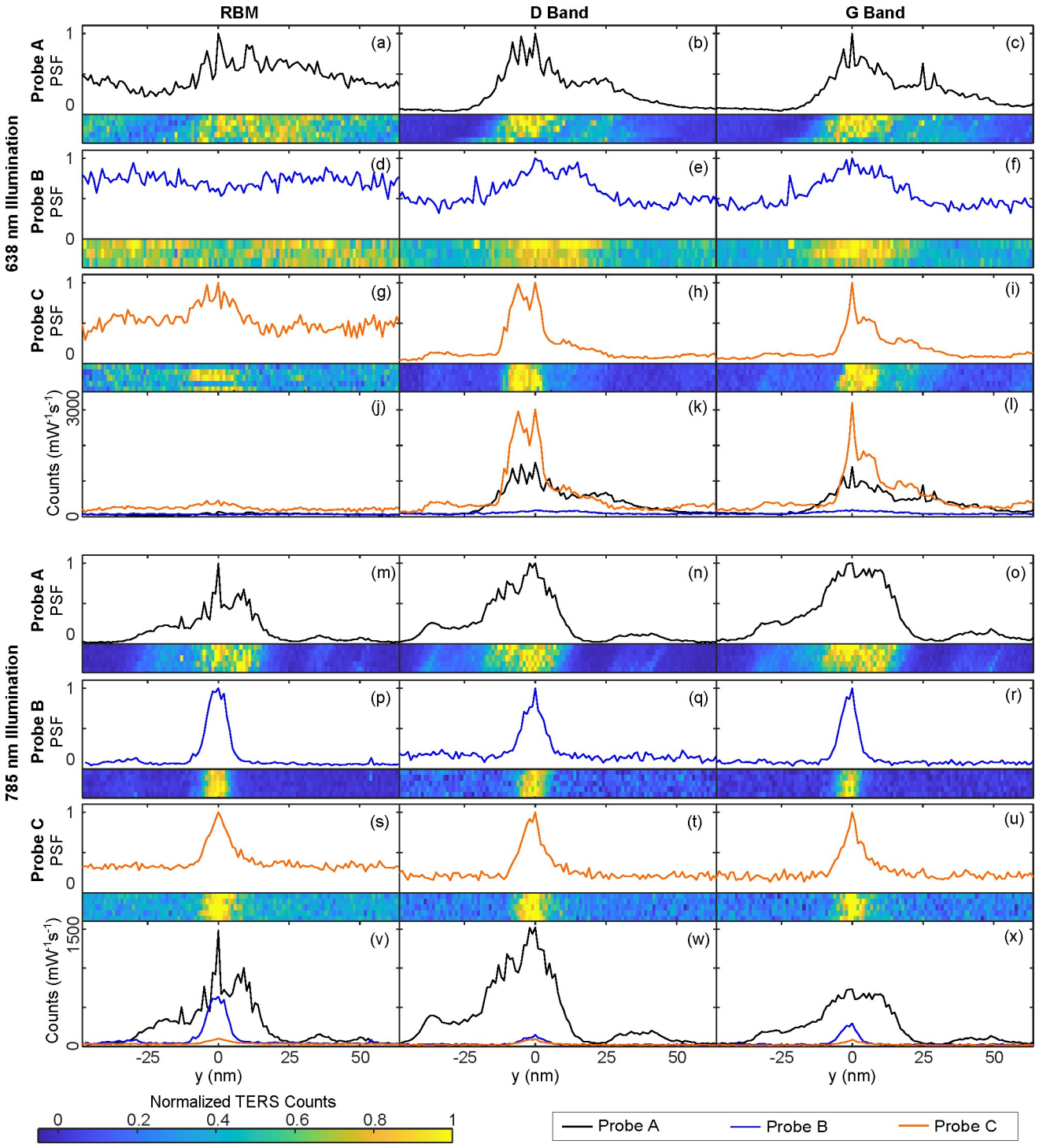

Figure 5. Data acquired from high-resolution cross section TERS maps of SWCNTs. PSFs with the corresponding normalized TERS map shown below for (a−i) 638 nm and (m−u) 785 nm illumination. Results are included for three TERS probes at the RBM, D-band, and G-band. SWCNT cross sections with TERS counts per mW of laser power per second of pixel acquisition time for (j−l) 638 nm and (v−x) 785 nm illumination. The PSFs are used to calculate the contrast and spot diameter of each TERS probe, which are summarized in Table 3.

measured contrast will depend on the tip−sample geometry.[28] Thus, the method presented here is suitable for the comparison of the performance of TERS probes in a specific microscope but likely not between different microscopes.

The plasmon response of grainy metal probes is highly dependent on random grain formation at the tip apex.[18,19,61] Hence, a statistical analysis of several probes is required for a comprehensive analysis of design parameters.

The relative intensities of the D-band and G-band have been shown to vary along the length of a SWCNT.[50] The method presented in this Article accounts for this by averaging five cross sections over a length of 5 nm. The method could be improved by averaging over more lines and a larger length. Furthermore, the method presented assumes a PSF that is symmetrical in the x−y planes. The 2D PSF could be

https://doi.org/10.1021/acsanm.2c01274
ACS Appl. Nano Mater. 2022, 5, 9024−9033

Table 3. Performance Characteristics of TERS Probes for Imaging SWCNTs at 638 and 785 nm Laser Excitations[a]

probe	wavelength (nm)	contrast RBM	contrast D	contrast G	contrast mean	spot diameter (nm)	apex diameter (nm)
A	638	N/A	13.59	9.82	11.21	57	430
	785	24.61	44.11	21.13	30.62	52	
B-1	638	N/A	1.13	1.39	1.26	45	147
B-2	785	13.73	3.62	7.23	8.19	16	
C-1	638	1.14	9.48	7.68	8.58	28	203
C-2	785	2.04	3.80	3.65	3.17	20	

[a]The apex diameter was estimated using the SEM data with separate probes.

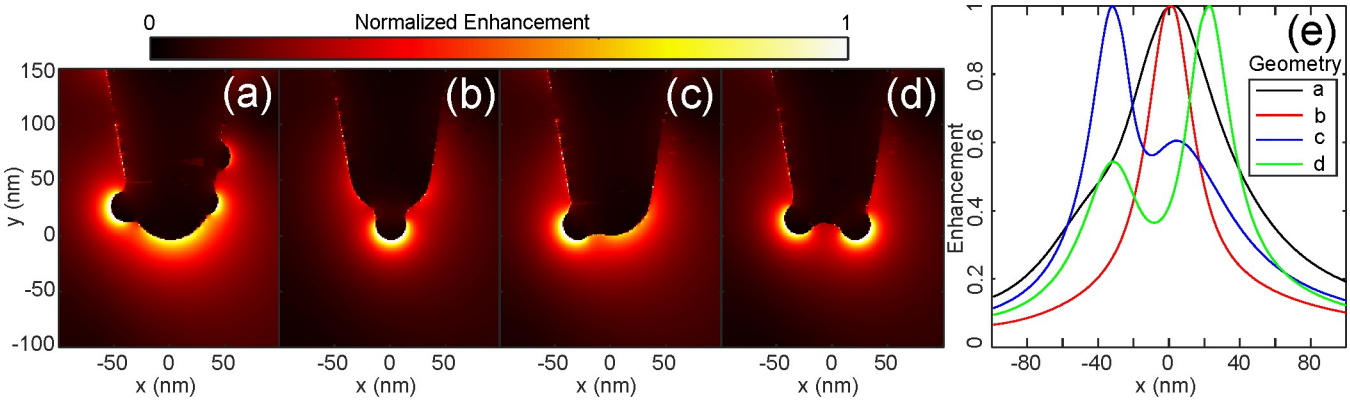

Figure 6. (a-d) Normalized enhancement maps of grainy silver probes acquired using boundary element method simulations. These geometries are used to investigate the effects of random grain formation on the spot diameter and introduction of multiple peaks in the PSF. (e) Normalized enhancement cross sections below the grainy silvers TERS probes shown in (a-d). Probes with multiple grains offset from the tip apex result in an increased spot diameter and multiple enhancement peaks that introduce artifacts into TERS maps.

calculated by devolving the PSF acquired with SWCNTS aligned with the *x*-axis and *y*-axis.

The proposed method of comparing probe imaging performance has been demonstrated on probes A, B, and C, which reveals the PSF, contrast, and spot diameter. The PSFs provide information about potential imaging artifacts due to multiple hot spots. The TERS imaging performance is characterized by acquiring a single TERS map, which does not require assumptions about particle density, apex diameter, or spot diameter. Therefore, this Article describes an improved method for the characterization of the imaging performance of a TERS probe compared to other methods in the literature that estimate the far-field[36−39] or near-field[36,37] spot sizes and calculate the enhancement using tip-in-contact and tip-retracted spectra or require the number of molecules in the scattering volume to be estimated.[38] The disadvantages of the method presented are that the measured contrast may be polarization dependent and that the spot diameter should be larger than the nanotube diameter.

A potential alternative method has been presented theoretically in the literature that uses the TERS approach curve on an ideal two-dimensional scattering surface. The tip radius is also measured using a topographic alignment grid.[62] This approach may provide characterization of TERS systems with reduced sample dependence but has not been confirmed experimentally.

Effects of Random Grain Formation. This section describes the effects of random grain formation on the electric field distribution at the tip apex. The simulated geometries do not approximate the probes shown in Figure 4 and are instead exaggerated examples that explain the formation of multiple peaks or broadening of a PSF.

Figure 6a−d shows the normalized electric field enhancement at the apex of simulated TERS probes with a 40 nm diameter tip apex and random grain formation. The probes are illuminated with a 638 nm planewave polarized in the *y*-axis. Figure 6e shows the normalized electric field cross section perpendicular to the apex corresponding to the geometries (in panels a−d).

Figure 6a shows a probe where no random grains have formed in the local vicinity of the tip apex. The corresponding cross section reveals that this configuration results in a wide spot diameter, which would lead to poor spatial resolution when used for TERS imaging.

Figure 6b shows a probe where a single grain has formed at the tip apex, acting as a new geometric apex. The corresponding cross section shows that this configuration results in the narrowest spot diameter and would be suitable for high-resolution TERS imaging.

Figure 6c shows a probe where a single grain has formed but is offset from the apex. The corresponding cross section reveals that this configuration results in an increased spot diameter. In addition, multiple enhancement peaks would introduce artifacts into TERS maps. These effects are amplified when multiple grains are offset from the apex as shown in Figure 6d and the corresponding cross section.

These results indicate that random grain formation has a profound effect on the performance of the TERS probes in terms of spot diameter and the introduction of artifacts in TERS maps due to multiple enhancement sites. Random grain formation provides an explanation for the different PSFs and spot diameters measured for probes B-1 and B-2 (see Table 3). The probe used with 638 nm illumination likely had multiple grains in proximity to the apex, resulting in a spot diameter of 45 nm and multiple PSF peaks. Meanwhile, the probe used

https://doi.org/10.1021/acsanm.2c01274
ACS Appl. Nano Mater. 2022, 5, 9024−9033

with 785 nm illumination likely had fewer or even a single grain at the apex resulting in a spot diameter of 16 nm and a single PSF peak.

One method of overcoming the random grain formation at the apex of TERS probes involves using a single nanoparticle as the plasmonic nanoantenna. Such probes can have a nanoparticle with dimensions optimized using optical simulations.[10] Using focused ion beam milling or deposition allows these nanoparticles to be created on AFM cantilevers for TERS imaging.[16,17] The methods of measuring probe performance outlined in this work will allow one to make a comparison between single nanoparticle TERS probes and the existing grainy metal layer TERS probes investigated here.

■ CONCLUSION

This Article describes a method for the measurement of the PSF, contrast, and spot diameter of TERS probes in the side-illumination configuration. Knowledge of the contrast and spot diameter allow probe characteristics to be matched to a given imaging application. For example, probes that provide low contrast and a small spot diameter are suitable for high-resolution imaging of small structures where the acquisition time can be increased without introducing significant optical drift. On the other hand, a probe that provides high contrast is suitable for large TERS maps where the acquisition time must be kept low to reduce optical drift. The method presented is unique, as using 785 nm excitation of the RBM allows for the selection of isolated SWCNTs that act as one-dimensional Raman scattering probes. This ensures accurate measurements of the near-field spot diameter for TERS probes. Different lasers can then be used to determine performance over a range of illumination wavelengths.

■ ASSOCIATED CONTENT

Supporting Information

The Supporting Information is available free of charge at https://pubs.acs.org/doi/10.1021/acsanm.2c01274.

Flowchart explaining the process used to align the optical system and acquire TERS maps (Figure S1); probe phase map that is used to align the laser to the probe apex and is a part of the standard operating procedure for the microscope (Figure S2); flowchart explaining the data processing method (Figure S3) (PDF)

■ AUTHOR INFORMATION

Corresponding Author

Luke R. McCourt − *The University of Newcastle, Callaghan, New South Wales 2308, Australia;* orcid.org/0000-0003-0593-6054; Email: Luke.Mccourt@uon.edu.au

Authors

Ben S. Routley − *The University of Newcastle, Callaghan, New South Wales 2308, Australia*

Michael G. Ruppert − *The University of Newcastle, Callaghan, New South Wales 2308, Australia*

Vicki J. Keast − *The University of Newcastle, Callaghan, New South Wales 2308, Australia*

C. I. Sathish − *Global Innovative Center for Advanced Nanomaterials (GICAN), College of Engineering, Science and Environment, University of Newcastle, Callaghan, New South Wales 2308, Australia*

Rohan Borah − *The University of Newcastle, Callaghan, New South Wales 2308, Australia*

Renee V. Goreham − *The University of Newcastle, Callaghan, New South Wales 2308, Australia*

Andrew J. Fleming − *The University of Newcastle, Callaghan, New South Wales 2308, Australia*

Complete contact information is available at: https://pubs.acs.org/10.1021/acsanm.2c01274

Notes

The authors declare no competing financial interest.

■ ACKNOWLEDGMENTS

This project was supported by the Australian Research Council Discovery Project DP210103383.

■ REFERENCES

(1) Hartschuh, A.; Sánchez, E. J.; Xie, X. S.; Novotny, L. High-Resolution Near-Field Raman Microscopy of Single-Walled Carbon Nanotubes. *Phys. Rev. Lett.* **2003**, *90*, 095503.

(2) Furukawa, H.; Kawata, S. Local Field Enhancement with an Apertureless Near-Field-Microscope Probe. *Opt. Commun.* **1998**, *148*, 221−224.

(3) Raether, H. *Surface Plasmons on Smooth and Rough Surfaces and on Gratings*; Springer, 1988; pp 4−39.

(4) Pelton, M.; Bryant, G. W. *Introduction to Metal-Nanoparticle Plasmonics*; John Wiley & Sons, 2013; Vol. 5; pp xi−xii.

(5) Stöckle, R. M.; Suh, Y. D.; Deckert, V.; Zenobi, R. Nanoscale Chemical Analysis by Tip-Enhanced Raman Spectroscopy. *Chem. Phys. Lett.* **2000**, *318*, 131−136.

(6) Hayazawa, N.; Inouye, Y.; Sekkat, Z.; Kawata, S. Near-Field Raman Scattering Enhanced by a Metallized Tip. *Chem. Phys. Lett.* **2001**, *335*, 369−374.

(7) Schmid, T.; Opilik, L.; Blum, C.; Zenobi, R. Nanoscale Chemical Imaging Using Tip-Enhanced Raman Spectroscopy: A Critical Review. *Angew. Chem., Int. Ed.* **2013**, *52*, 5940−5954.

(8) Alastair Smith, D.; Webster, S.; Ayad, M.; Evans, S. D.; Fogherty, D.; Batchelder, D. Development of a Scanning Near-Field Optical Probe for Localised Raman Spectroscopy. *Ultramicroscopy* **1995**, *61*, 247−252.

(9) Böhme, R.; Cialla, D.; Richter, M.; Rösch, P.; Popp, J.; Deckert, V. Biochemical Imaging below the Diffraction Limit − Probing Cellular Membrane Related Structures by Tip-Enhanced Raman Spectroscopy (TERS). *Journal of Biophotonics* **2010**, *3*, 455−461.

(10) McCourt, L. R.; Ruppert, M. G.; Routley, B. S.; Indirathankam, S. C.; Fleming, A. F. A Comparison of Gold and Silver Nanocones and Geometry Optimisation for Tip-Enhanced Microscopy. *J. Raman Spectrosc.* **2020**, *51*, 2208−2216.

(11) Cao, Y.; Sun, M. Tip-Enhanced Raman Spectroscopy. *Reviews in Physics* **2022**, *8*, 100067.

(12) Wiley, B. J.; Im, S. H.; Li, Z.-Y.; McLellan, J.; Siekkinen, A.; Xia, Y. Maneuvering the Surface Plasmon Resonance of Silver Nanostructures through Shape-Controlled Synthesis. *J. Phys. Chem. B* **2006**, *110*, 15666−15675.

(13) Verma, P. Tip-Enhanced Raman Spectroscopy: Technique and Recent Advances. *Chem. Rev.* **2017**, *117*, 6447−6466.

(14) Huang, T.-X.; Li, C.-W.; Yang, L.-K.; Zhu, J.-F.; Yao, X.; Liu, C.; Lin, K.-Q.; Zeng, Z.-C.; Wu, S.-S.; Wang, X.; Yang, F.-Z.; Ren, B. Rational Fabrication of Silver-Coated AFM TERS Tips with a High Enhancement and Long Lifetime. *Nanoscale* **2018**, *10*, 4398−4405.

(15) Hermann, R. J.; Gordon, M. J. Quantitative Comparison of Plasmon Resonances and Field Enhancements of Near-Field Optical Antennae Using FDTD Simulations. *Opt. Express* **2018**, *26*, 27668−27682.

(16) Vasconcelos, T. L.; Archanjo, B. S.; Oliveira, B. S.; Silva, W. F.; Alencar, R. S.; Rabelo, C.; Achete, C. A.; Jorio, A.; Cançado, L. G.

Optical Nanoantennas for Tip-Enhanced Raman Spectroscopy. *IEEE J. Sel. Top. Quantum Electron.* **2021**, *27*, 1−11.
(17) Fleischer, M.; Weber-Bargioni, A.; Altoe, M. V. P.; Schwartzberg, A. M.; Schuck, P. J.; Cabrini, S.; Kern, D. P. Gold Nanocone Near-Field Scanning Optical Microscopy Probes. *ACS Nano* **2011**, *5*, 2570−2579.
(18) Taguchi, A.; Yu, J.; Verma, P.; Kawata, S. Optical Antennas with Multiple Plasmonic Nanoparticles for Tip-Enhanced Raman Microscopy. *Nanoscale* **2015**, *7*, 17424−17433.
(19) Asghari-Khiavi, M.; Wood, B. R.; Hojati-Talemi, P.; Downes, A.; McNaughton, D.; Mechler, A. Exploring the Origin of Tip-Enhanced Raman Scattering; Preparation of Efficient TERS Probes with High Yield. *J. Raman Spectrosc.* **2012**, *43*, 173−180.
(20) Ma, J.; Song, J.; Cheng, Y.; Sun, M. Plexciton and Electron−Phonon Interaction in Tip-Enhanced Resonance Raman Scattering. *J. Raman Spectrosc.* **2021**, *52*, 1685−1697.
(21) Ma, J.; Cheng, Y.; Sun, M. Plexcitons, Electric Field Gradient and Electron−Phonon Coupling in Tip-Enhanced Raman Spectroscopy (TERS). *Nanoscale* **2021**, *13*, 10712−10725.
(22) Zhang, R.; Zhang, Y.; Dong, Z. C.; Jiang, S.; Zhang, C.; Chen, L. G.; Zhang, L.; Liao, Y.; Aizpurua, J.; Luo, Y.; Yang, J. L.; Hou, J. G. Chemical Mapping of a Single Molecule by Plasmon-Enhanced Raman Scattering. *Nature* **2013**, *498*, 82−86.
(23) Zhang, W.; Yeo, B. S.; Schmid, T.; Zenobi, R. Single Molecule Tip-Enhanced Raman Spectroscopy with Silver Tips. *J. Phys. Chem. C* **2007**, *111*, 1733−1738.
(24) Stadler, J.; Oswald, B.; Schmid, T.; Zenobi, R. Characterizing Unusual Metal Substrates for Gap-Mode Tip-Enhanced Raman Spectroscopy. *J. Raman Spectrosc.* **2013**, *44*, 227−233.
(25) Meng, L.; Wang, Y.; Gao, M.; Sun, M. Electromagnetic Field Gradient-Enhanced Raman Scattering in TERS Configurations. *J. Phys. Chem. C* **2021**, *125*, 5684−5691.
(26) Rahaman, M.; Milekhin, A. G.; Mukherjee, A.; Rodyakina, E. E.; Latyshev, A. V.; Dzhagan, V. M.; Zahn, D. R. T. The Role of a Plasmonic Substrate on the Enhancement and Spatial Resolution of Tip-Enhanced Raman Scattering. *Faraday Discuss.* **2019**, *214*, 309−323.
(27) Sivadasan, A. K.; Patsha, A.; Maity, A.; Chini, T. K.; Dhara, S. Effect of Scattering Efficiency in the Tip-Enhanced Raman Spectroscopic Imaging of Nanostructures in the Sub-diffraction Limit. *J. Phys. Chem. C* **2017**, *121*, 26967−26975.
(28) Duesberg, G. S.; Loa, I.; Burghard, M.; Syassen, K.; Roth, S. Polarized Raman Spectroscopy on Isolated Single-Wall Carbon Nanotubes. *Phys. Rev. Lett.* **2000**, *85*, 5436−5439.
(29) Jorio, A.; Santos, A. P.; Ribeiro, H. B.; Fantini, C.; Souza, M.; Vieira, J. P. M.; Furtado, C. A.; Jiang, J.; Saito, R.; Balzano, L.; Resasco, D. E.; Pimenta, M. A. Quantifying Carbon-Nanotube Species with Resonance Raman Scattering. *Phys. Rev. B* **2005**, *72*, 075207.
(30) Sfeir, M. Y.; Beetz, T.; Wang, F.; Huang, L.; Huang, X. M. H.; Huang, M.; Hone, J.; O'Brien, S.; Misewich, J. A.; Heinz, T. F.; Wu, L.; Zhu, Y.; Brus, L. E. Optical Spectroscopy of Individual Single-Walled Carbon Nanotubes of Defined Chiral Structure. *Science* **2006**, *312*, 554−556.
(31) Kumar, N.; Su, W.; Vesely, M.; Weckhuysen, B. M.; Pollard, A. J.; Wain, A. J. Nanoscale Chemical Imaging of Solid−Liquid Interfaces Using Tip-Enhanced Raman Spectroscopy. *Nanoscale* **2018**, *10*, 1815−1824.
(32) Routley, B. S.; Holdsworth, J. L.; Fleming, A. J. Optimization of Near-Field Scanning Optical Lithography. In *Proc. SPIE 9423, Alternative Lithographic Technologies VII*, San Jose, California, 2015; Vol. *9423*, pp 94230F.
(33) Gersten, J. I. The Effect of Surface Roughness on Surface Enhanced Raman Scattering. *J. Chem. Phys.* **1980**, *72*, 5779−5780.
(34) Zhang, W.; Cui; Yeo, B.-S.; Schmid, T.; Hafner, C.; Zenobi, R. Nanoscale Roughness on Metal Surfaces Can Increase Tip-Enhanced Raman Scattering by an Order of Magnitude. *Nano Lett.* **2007**, *7*, 1401−1405.
(35) Steidtner, J.; Pettinger, B. High-Resolution Microscope for Tip-Enhanced Optical Processes in Ultrahigh Vacuum. *Rev. Sci. Instrum.* **2007**, *78*, 103104.
(36) Hayazawa, N.; Inouye, Y.; Sekkat, Z.; Kawata, S. Metallized Tip Amplification of Near-Field Raman Scattering. *Opt. Commun.* **2000**, *183*, 333−336.
(37) Hayazawa, N.; Yano, T.; Watanabe, H.; Inouye, Y.; Kawata, S. Detection of an Individual Single-Wall Carbon Nanotube by Tip-Enhanced near-Field Raman Spectroscopy. *Chem. Phys. Lett.* **2003**, *376*, 174−180.
(38) Roy, D.; Wang, J.; Williams, C. Novel Methodology for Estimating the Enhancement Factor for Tip-Enhanced Raman Spectroscopy. *J. Appl. Phys.* **2009**, *105*, 013530.
(39) Sonntag, M. D.; Klingsporn, J. M.; Garibay, L. K.; Roberts, J. M.; Dieringer, J. A.; Seideman, T.; Scheidt, K. A.; Jensen, L.; Schatz, G. C.; Van Duyne, R. P. Single-Molecule Tip-Enhanced Raman Spectroscopy. *J. Phys. Chem. C* **2012**, *116*, 478−483.
(40) Pettinger, B.; Picardi, G.; Schuster, R.; Ertl, G. Surface Enhanced Raman Spectroscopy: Towards Single Molecule Spectroscopy. *Electrochemistry* **2000**, *68*, 942−949.
(41) Pettinger, B.; Schambach, P.; Villagómez, C. J.; Scott, N. Tip-Enhanced Raman Spectroscopy: Near-Fields Acting on a Few Molecules. *Annu. Rev. Phys. Chem.* **2012**, *63*, 379−399.
(42) Rossmann, K. Point Spread-Function, Line Spread-Function, and Modulation Transfer Function. *Radiology* **1969**, *93*, 257−272.
(43) Kuzmany, H.; Plank, W.; Hulman, M.; Kramberger, C.; Grüneis, A.; Pichler, T.; Peterlik, H.; Kataura, H.; Achiba, Y. Determination of SWCNT Diameters from the Raman Response of the Radial Breathing Mode. *European Physical Journal B - Condensed Matter and Complex Systems* **2001**, *22*, 307−320.
(44) McEuen, P.; Fuhrer, M.; Park, H. Single-Walled Carbon Nanotube Electronics. *IEEE Transactions on Nanotechnology* **2002**, *1*, 78−85.
(45) Araujo, P. T.; Maciel, I. O.; Pesce, P. B. C.; Pimenta, M. A.; Doorn, S. K.; Qian, H.; Hartschuh, A.; Steiner, M.; Grigorian, L.; Hata, K.; Jorio, A. Nature of the Constant Factor in the Relation between Radial Breathing Mode Frequency and Tube Diameter for Single-Wall Carbon Nanotubes. *Phys. Rev. B* **2008**, *77*, 241403.
(46) Jorio, A.; Saito, R.; Hafner, J. H.; Lieber, C. M.; Hunter, M.; McClure, T.; Dresselhaus, G.; Dresselhaus, M. S. Structural (n, m) Determination of Isolated Single-Wall Carbon Nanotubes by Resonant Raman Scattering. *Phys. Rev. Lett.* **2001**, *86*, 1118−1121.
(47) Souza Filho, A. G.; Chou, S. G.; Samsonidze, G. G.; Dresselhaus, G.; Dresselhaus, M. S.; An, L.; Liu, J.; Swan, A. K.; Ünlü, M. S.; Goldberg, B. B.; Jorio, A.; Grüneis, A.; Saito, R. Stokes and Anti-Stokes Raman Spectra of Small-Diameter Isolated Carbon Nanotubes. *Phys. Rev. B* **2004**, *69*, 115428.
(48) Ajiki, H.; Ando, T. Aharonov-Bohm Effect in Carbon Nanotubes. *Physica B: Condensed Matter* **1994**, *201*, 349−352.
(49) Araujo, P.; Pesce, P.; Dresselhaus, M.; Sato, K.; Saito, R.; Jorio, A. Resonance Raman Spectroscopy of the Radial Breathing Modes in Carbon Nanotubes. *Physica E: Low-dimensional Systems and Nanostructures* **2010**, *42*, 1251−1261.
(50) Chen, C.; Hayazawa, N.; Kawata, S. A 1.7 Nm Resolution Chemical Analysis of Carbon Nanotubes by Tip-Enhanced Raman Imaging in the Ambient. *Nat. Commun.* **2014**, *5*, 3312.
(51) Hartschuh, A.; Anderson, N.; Novotny, L. Near-Field Raman Spectroscopy Using a Sharp Metal Tip. *J. Microsc.* **2003**, *210*, 234−240.
(52) Keast, V. J. Corrosion Processes of Silver Nanoparticles. *Applied Nanoscience* **2022**, *12*, 1859−1868.
(53) Keast, V. J.; Myles, T. A.; Shahcheraghi, N.; Cortie, M. B. Corrosion Processes of Triangular Silver Nanoparticles Compared to Bulk Silver. *J. Nanopart. Res.* **2016**, *18*, 45.
(54) Oates, T. W. H.; Losurdo, M.; Noda, S.; Hinrichs, K. The Effect of Atmospheric Tarnishing on the Optical and Structural Properties of Silver Nanoparticles. *J. Phys. D: Appl. Phys.* **2013**, *46*, 145308.

https://doi.org/10.1021/acsanm.2c01274
ACS Appl. Nano Mater. 2022, 5, 9024−9033

(55) McMahon, M.; Lopez, R.; Meyer, H.; Feldman, L.; Haglund, R. Rapid Tarnishing of Silver Nanoparticles in Ambient Laboratory Air. *Appl. Phys. B: Laser Opt.* **2005**, *80*, 915−921.
(56) Hohenester, U.; Trügler, A. MNPBEM − A Matlab Toolbox for the Simulation of Plasmonic Nanoparticles. *Comput. Phys. Commun.* **2012**, *183*, 370−381.
(57) Pettinger, B.; Ren, B.; Picardi, G.; Schuster, R.; Ertl, G. Tip-Enhanced Raman Spectroscopy (TERS) of Malachite Green Isothiocyanate at Au(111): Bleaching Behavior under the Influence of High Electromagnetic Fields. *J. Raman Spectrosc.* **2005**, *36*, 541−550.
(58) Nelayah, J.; Kociak, M.; Stéphan, O.; García de Abajo, F. J.; Tencé, M.; Henrard, L.; Taverna, D.; Pastoriza-Santos, I.; Liz-Marzán, L. M.; Colliex, C. Mapping Surface Plasmons on a Single Metallic Nanoparticle. *Nat. Phys.* **2007**, *3*, 348−353.
(59) Wu, Y.; Li, G.; Camden, J. P. Probing Nanoparticle Plasmons with Electron Energy Loss Spectroscopy. *Chem. Rev.* **2018**, *118*, 2994−3031.
(60) Lee, J.; Crampton, K. T.; Tallarida, N.; Apkarian, V. Visualizing Vibrational Normal Modes of a Single Molecule with Atomically Confined Light. *Nature* **2019**, *568*, 78−82.
(61) Taguchi, A. Plasmonic Tip for Nano Raman Microcopy: Structures, Materials, and Enhancement. *Optical Review* **2017**, *24*, 462−469.
(62) Neto, A. R.; Rabelo, C.; Cançado, L. G.; Engel, M.; Steiner, M.; Jorio, A. Protocol and Reference Material for Measuring the Nanoantenna Enhancement Factor in Tip-enhanced Raman Spectroscopy. In *2019 4th International Symposium on Instrumentation Systems, Circuits and Transducers (INSCIT)*, 2019; pp 1−6.

Recommended by ACS

Carbon Nanotubes Coupled with Silica Toroid Microcavities as Emitters for Silicon-Integrated Photonics

Ren Tokunaga, Hideyuki Maki, *et al.*

OCTOBER 11, 2022
ACS APPLIED NANO MATERIALS
READ

Multiwavelength Photothermal Imaging of Individual Single-Walled Carbon Nanotubes Suspended in a Solvent

Jun Miyazaki, Ryosuke Kondo, *et al.*

AUGUST 04, 2022
THE JOURNAL OF PHYSICAL CHEMISTRY A
READ

Efficient Inner-to-Outer Wall Energy Transfer in Highly Pure Double-Wall Carbon Nanotubes Revealed by Detailed Spectroscopy

Maksiem Erkens, Sofie Cambré, *et al.*

SEPTEMBER 27, 2022
ACS NANO
READ

Electroluminescence from Single-Walled Carbon Nanotubes with Quantum Defects

Min-Ken Li, Ralph Krupke, *et al.*

JUNE 22, 2022
ACS NANO
READ

Get More Suggestions >

https://doi.org/10.1021/acsanm.2c01274
ACS Appl. Nano Mater. 2022, 5, 9024−9033